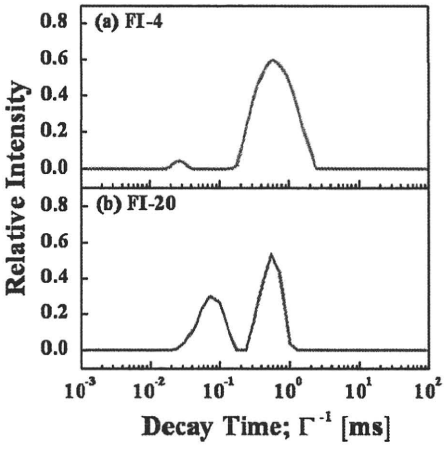

FIG. 4. (Color online) Decay time distribution functions of (a) FI-4 and (b) FI-20 at 25 °C.

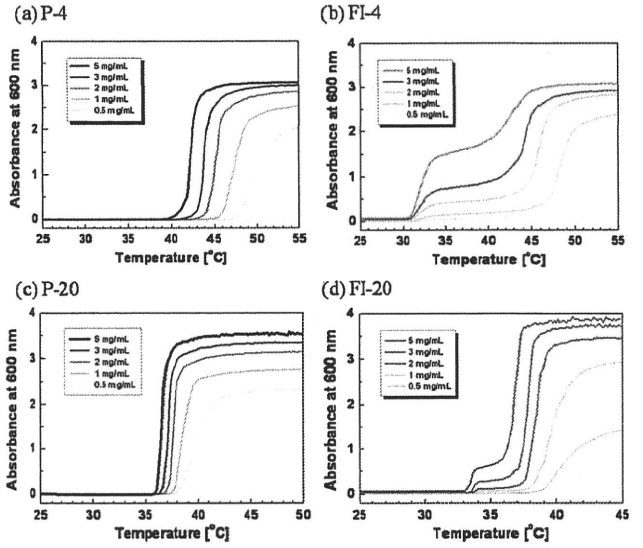

FIG. 5. (Color online) Temperature dependence of optical transmittance at 600 nm of (a) P-4, (b) FI-4, (c) P-20, and (d) FI-20, in aqueous solutions at a concentration of 5.0 mg/ml and heating rate of 0.2 °C/min.

peak, whereas the GPC curve for FI-4 showed the presence of two peaks. As shown in Fig. 2, from the GPC measurement for FI-4 with RI using THF as the mobile phase, only one peak was observed, similar to that of P-4 using ultrapure water as the mobile phase. The FI-4 peak that eluted at approximately the same time as that of P-4 was assigned to the unimer, namely, a PIPAAm-C_{60} (FI-4) molecule. The primary peak of FI-4, which eluted at an earlier time than that of P-4, indicated the existence of a species with a higher molecular weight than a single FI-4 molecule and would correspond to a molecular assembly of FI-4. It was suggested that the molecular assembly of FI-4 formed a core-shell micelle structure composed of an inner core of C_{60} molecules and an outer shell layer of PIPAAm chains, below the LCST of FI-4, resulting from intermolecular hydrophobic interactions between C_{60} molecules in water. Therefore, for FI-4, the unimer and the molecular assembly coexisted in water at 25 °C. Similar to P-4, the GPC curve for P-20 showed the presence of only one peak and the GPC curve for FI-20 showed the presence of two peaks. However, the primary peak of FI-20, which eluted earlier than that of P-20, was slight. This indicated that the amount of the molecular assembly tended to decrease with increasing polymer chain length in PIPAAm-C_{60}. A longer polymer chain would give rise to a decrease in intermolecular hydrophobic interactions among C_{60} molecules due to the decrease in the C_{60} contents, and increases the polymer wrapping effects to C_{60} molecules through a charge-transfer complexation with polymers containing a carbonyl group.[21–23]

From DLS measurements on both FI-4 and FI-20 at 20 °C (below each LCST), two decay modes were observed in the decay time distribution, as shown in Fig. 4. The first and slow modes of FI-4 correspond to hydrodynamic radius (R_h) values of 4.7 and 87.3 nm, respectively, whereas those of FI-20 correspond to 9.5 and 83.0 nm, respectively. In view of the GPC results, it is inferred that the first mode is ascribed to the unimeric FI-4 and FI-20, whereas the slow mode is associated with the molecular assembly of FI-4 and FI-20. Consequently, from the DLS measurements, it was also confirmed that the unimer and molecular assembly of PIPAAm-C_{60} coexist in water below their LCSTs.

C. Effect of the chain length of PIPAAm on the thermal transitions of PIPAAm-C_{60}

The absorbance changes in FI-4 and FI-20 at various concentrations of the PIPAAm-C_{60} aqueous solutions in response to temperature, compared to that of P-4 and P-20 are shown in Fig. 5. For P-4 and P-20, the one-step absorbance change of the aqueous solution was observed in response to increasing temperature at a rate of 0.2 °C/min from 25 to 55 °C, regardless of the concentration. However, the temperature at the onset of the absorbance change shifted lower with an increase in the concentration of P-4 and P-20, on the basis of the changes in the polymer-solvent interaction.[24] On the other hand, for both FI-4 and FI-20, two-step absorbance changes were observed in response to temperature. Interestingly, the temperature at the primary onset of the rapid absorbance change was approximately constant, independent of the PIPAAm-C_{60} concentration, whereas the temperature at the second onset was dependent on the PIPAAm-C_{60} concentration in the same manner as with P-4 and P-20. In view of these observed concentration effects, the first and second phase transitions of these PIPAAm-C_{60} solutions are suggested to be associated with aggregation of the molecular assembly and unimer of PIPAAm-C_{60}, respectively.

For chain length effects, the magnitude of the first-step change in the absorbency of FI-4 was larger than that of FI-20, but the magnitude of the second-step change was smaller. However, the temperature at the second onset of FI-4 was higher than that of FI-20. In correlation with this behavior, Xia *et al.*[15] reported that the LCST of a PIPAAm chain synthesized by ATRP shifted lower with increasing

molecular weight of PIPAAm. These findings indicate that the second-step change in absorbance is brought about by aggregation of the unimeric PIPAAm-C_{60}.

In regard to the reversibility, the transmittance changes in the PIPAAm-C_{60} solution were measured in response to reversible temperature changes across the LCST. Increasing the temperature, the PIPAAm-C_{60} solution was turbid, and then, the transmittance was restored by cooling (see Fig S2 in supporting information).[20] The transmittance profile in response to reversible temperature changes possessed the hysteresis property. Interestingly, the PIPAAm-C_{60} with shorter polymer chain showed the transmittance profile with the larger hysteresis in response to reversible temperature changes (data not shown). The detail of the hysteresis will be described elsewhere.

Here, it should be noted that although unreacted PIPAAm-Cl might exist in scarce amounts in the PIPAAm-C_{60} system, it is difficult to completely remove this component because of the same characteristics of both PIPAAm-Cl and PIPAAm-C_{60}. However, we believe that the unreacted PIPAAm-Cl, namely, free polymer chain, would not trigger the two-step phase transition behavior of the PIPAAm-C_{60}. As a verification experiment for this, the transmittance changes in the mixture solution of micelle comprised of poly[styrene-*block*-(*N*-isopropylacrylamide-*co*-*N*, *N'*-dimethylacrylamide)] [PSt-*b*-P(IPAAm-*co*-DMAAm)] and free PIPAAm chain were measured in response to temperature changes (see Fig S3 in supporting information).[20] Consequently, the mixture showed not two separated phase transition but one sharp transition. The LCST of the mixture lied between that of pure micelle and pure free polymer, and was dependent on the weight ratio of polymer/micelle ($p:m$). The phase transition of the mixture containing free PIPAAm in a low dose was nearly identical with that of the pure micelle. The above result confirms our suggestion that free PIPAAm would not induce to the two-step phase transition in this PIPAAm-C_{60} system.

The foregoing results led us to conclude that the first and second phase transitions of these PIPAAm-C_{60} solutions are associated with the aggregation of the molecular assembly and unimer of PIPAAm-C_{60}, respectively. Moreover, this work demonstrates that the phase transition behavior of PIPAAm-C_{60} in water is controllable by varying the chain length of PIPAAm. Preliminary experiments have shown that the PIPAAm-C_{60} conjugates have effective bioactivities, such as superoxide generation by photoirradiation. Further studies are continuing in our group and will be published in due course.

IV. CONCLUSIONS

Thermoresponsive conjugates PIPAAm-C_{60} comprising a C_{60} molecule and a PIPAAm chain as a thermoresponsive segment with varying chain lengths were synthesized by ATRP polymerization. Unimeric PIPAAm-C_{60} and a micellelike molecular assembly of PIPAAm-C_{60} coexisted in the PIPAAm-C_{60} aqueous solution below their LCSTs. The existence ratio of the molecular assembly to the unimer in the PIPAAm-C_{60} aqueous solution decreased with an increase in the chain length of PIPAAm. The PIPAAm-C_{60} aqueous solution showed two-step phase transitions associated with aggregation of the molecular assembly and the unimer in response to temperature. The chain length of PIPAAm was found to be the predominant factor involved in the solution characteristics of PIPAAm-C_{60}. Consequently, the PIPAAm-C_{60} is expected to be an intelligent biomaterial possessing heat-induced accumulation and bioactivities.

ACKNOWLEDGMENT

This work was supported in part by a Grant-in-Aid from the *Green Research Center for Photo-Science and Technology* of the Tokyo University of Science.

[1]P. J. Krusic, E. Wasserman, P. N. Keizer, J. R. Morton, and K. F. Preston, Science **254**, 1183 (1991).
[2]L. L. Dugan *et al.*, Proc. Natl. Acad. Sci. U.S.A. **94**, 9434 (1997).
[3]S. H. Friedman, D. L. Decamp, R. P. Sijbesma, G. Srdanov, F. Wudl, and G. L. Kenyon, J. Am. Chem. Soc. **115**, 6506 (1993).
[4]H. Tokuyama, S. Yamago, E. Nakamura, T. Shiraki, and Y. Sugiura, J. Am. Chem. Soc. **115**, 7918 (1993).
[5]Y. Tabata, Y. Murakami, and Y. Ikada, Jpn. J. Cancer Res. **88**, 1108 (1997).
[6]E. Nakamura and A. Isobe, Acc. Chem. Res. **36**, 807 (2003).
[7]L. Y. Chiang, J. B. Bhonsle, L. Wang, S. F. Shu, T. M. Chang, and J. R. Hwu, Tetrahedron **52**, 4963 (1996).
[8]M. Brettreich and A. Hirsch, Tetrahedron Lett. **39**, 2731 (1998).
[9]K. E. Geckeler, Trends Polym. Sci. **2**, 355 (1994).
[10]S. Yamago *et al.*, Chem. Biol. **2**, 385 (1995).
[11]A. Tamura, K. Uchida, and H. Yajima, Chem. Lett. **35**, 282 (2006).
[12]M. Heskins and J. E. Guillet, J. Macromol. Sci., Chem. **A2**, 1441 (1968).
[13]R. Yoshida, K. Sakai, T. Okano, and Y. Sakurai, J. Biomater. Sci., Polym. Ed. **6**, 585 (1995).
[14]R. Yoshida, K. Uchida, Y. Kaneko, K. Sakai, A. Kikuchi, Y. Sakurai, and T. Okano, Nature (London) **374**, 240 (1995).
[15]Y. Xia, X. Yin, N. A. D. Burke, and H. D. H. Stöver, Macromolecules **38**, 5937 (2005).
[16]Y. Xia, N. A. D. Burke, and H. D. H. Stöver, Macromolecules **39**, 227 (2006).
[17]M. Nakayama and T. Okano, Biomacromolecules **6**, 2320 (2005).
[18]J. E. Chung, M. Yokoyama, and T. Okano, J. Controlled Release **65**, 93 (2000).
[19]J. Queffelec, S. G. Gaynor, and K. Matyjaszewski, Macromolecules **33**, 8629 (2000).
[20]See supplementary material at http://dx.doi.org/10.1116/1.3319348 E-BJIOBN-5-002001 for details on three supplementary experimental data: (1) the 1H-NMR spectra of PIPAAm-Cl and PIPAAm-C_{60}, (2) the transmittance profile of PIPAAm-C_{60} in response to reversible temperature changes, and (3) the verification experiment of our suggestion that unreacted PIPAAm-Cl would not trigger the two-step phase transition behavior of the PIPAAm-C_{60}.
[21]M. L. Sushko, H. Tenhu, and S. I. Klenin, Polymer **43**, 2769 (2002).
[22]C. Ungurenasu and A. Airinei, J. Med. Chem. **43**, 3186 (2000).
[23]S. Dai, P. Ravi, C. H. Tan, and K. C. Tam, Langmuir **20**, 8569 (2004).
[24]D. G. Lessard, M. Ousalem, and X. X. Zhu, Can. J. Chem. **79**, 1870 (2001).

J Biorheol (2009) 23:64–71
DOI 10.1007/s12573-009-0002-3

BRIEF COMMUNICATION

Improved blood biocompatibility of composite film of chitosan/carbon nanotubes complex

Katsumune Takahashi · Rumi Shizume · Katsumi Uchida · Hirofumi Yajima

Received: 26 November 2008 / Accepted: 2 December 2008 / Published online: 8 April 2009
© Japanese Society of Biorheology 2009

Abstract Single-walled carbon nanotubes are novel molecular-scale wires having excellent anti-adhesion properties with regard to platelets. On the other hand, chitosan is a partially de-acetylated derivative of chitin that has a critical role in cell attachment and growth. The aim of this study was to investigate how carbon nanotubes improve the blood biocompatibility of chitosan film. We prepared composite films with various concentrations of chitosan/carbon nanotubes (CS/CNTs) (1.3–6.3 wt%). The sample surfaces were characterized by Raman spectroscopy, X-ray photoelectron spectroscopy (XPS), atomic force microscopy (AFM), and contact angle measurements. The surface characterization revealed that the surface of the CS/CNTs composite film became more hydrophobic with increasing amounts of CNTs. Cell attachment tests using bovine aortic endothelial cells (BAECs) indicated that CS/CNTs composite films retained their cell adhesion ability. The blood compatibility of the CS/CNTs composite films was evaluated using the blood platelet adhesion and activation tests in vitro. Platelet adhesion results confirmed that platelet adhesion and the formation of a platelet network were inhibited on composite films with higher concentrations of CNTs (5.1 wt%). Our experimental results show that the novel composite film containing CS/CNTs possesses two paradoxical characteristics, namely, good adherence of endothelial cells and minimum adherence and activation of platelets, making this film a promising antithrombogenic material for use in the biomedical field.

K. Takahashi · R. Shizume · K. Uchida · H. Yajima (✉)
Department of Applied Chemistry, Faculty of Science,
Tokyo University of Science, 12-1 Funagawara-machi,
Ichigaya, Shinjyuku-ku, Tokyo 162-0826, Japan
e-mail: yajima@rs.kagu.tus.ac.jp

Keywords Blood compatibility · Chitosan · Carbon nanotubes · Cell attachment · Surface characterization

Introduction

Antithrombogenic biomaterial is being extensively studied in order to fabricate artificial organs and biomaterials in contact with blood. A significant goal for the application of antithrombogenic biomaterial is to prevent thrombus formation on the material surface. Thrombus formation involves a process with multiple steps, including plasma protein adsorption, platelet adhesion and aggregation, and, finally, the activation of clotting factor. Properties of the surface such as hydrophobicity/hydrophilicity, surface charge, and roughness of biomaterials strongly influence blood platelet adhesion, activation, and thrombus formation when the surface is in contact with blood.

Chitin is a co-polymer of *N*-acetyl-glucosamine and *N*-glucosamine units randomly or block distributed throughout the biopolymer chain. Chitosan is the *N*-deacetylated derivative of chitin (Fig. 1), the second most abundant natural polysaccharide after cellulose. When the number of *N*-glucosamine units is higher, the polymer is termed chitosan. Commercially, chitin and chitosan are obtained from shellfish sources such as crabs and shrimps. Chitosan has been used in a wide variety of biomedical applications, such as wound dressing and bone healing materials, due to its biocompatibility and non-toxicity [1, 2]. Polysaccharides are expected to be effective biomedical materials because of the important role of saccharide moieties in cell signaling and immune recognition mechanisms [3]. However, chitosan promotes platelet adhesion, activation, and thrombus formation [4, 5]. This thrombogenic property has restricted

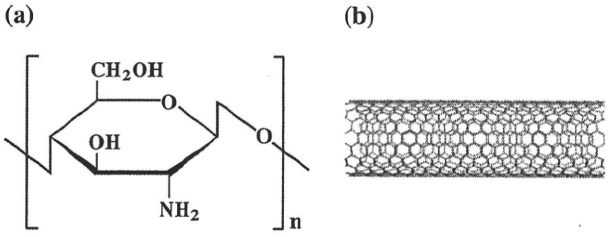

Fig. 1 The structures of (**a**) chitosan and (**b**) single-wall carbon nanotube

its application as a blood-contacting biomaterial. It is essential to modify the chitosan film when using it as the antithrombogenic biomaterial.

Carbon materials are known to be inert to cells and tissues because of their pure carbon compositions. Carbon nanotubes (CNTs), rolled graphite sheets with nanoscale diameters (Fig. 1), have attracted a significant amount of attention due to their unique properties, such as high hardness, low coefficient of friction, chemical inertness, high wear and corrosion resistance, which make CNTs excellent candidates for biocompatible coatings on implants. Recently, CNTs have been reported to have promising potential for biomedical applications such as photodynamic therapy for tumors, neuroscience research, and biosensor technology [6–9].

However, a serious problem with the CNTs' application to biomaterial is their poor dispersion in water or organic agent and facile aggregation in bundles due to its strong van der Waals forces. Takahashi et al. [10] found that polysaccharide chitosan was an efficient dispersion agent for CNTs under acidic conditions because CNTs were wrapped by chitosan molecules.

Therefore, CS/CNTs composite films should be ideal candidates for polymer biomaterials. The objective of this study was to investigate the surface properties of fabricated CS/CNTs composite film. Surface properties of prepared CS/CNTs films were analyzed by Raman spectroscopy, X-ray photoelectron spectroscopy (XPS), atomic force microscopy (AFM), and contact angle measurements. The cell attachment tests were carried out using bovine aortic endothelial cells (BAECs). The evaluation of blood compatibility was based on human blood platelet adhesion and platelet activation tests.

Materials and methods

Preparation of CS/CNTs films

Chitosan was provided by Kimica Corporation (DDA: 80–90%, Mw: 124 kDa). Chitosan solution was obtained by dissolving it in 2% acetic acid (15 mg/ml). CNTs were purchased from Carbon Nanotechnologies Inc. (HiPco-SWNTs). The CNTs were dispersed into chitosan solution (CNTs concentration: 1.3, 2.6, 3.8, 5.1, and 6.3 wt%). These solutions were ultrasonicated at 20 W for 1 h and then ultracentrifuged at 163,000g for 1 h to remove large bundled CNTs and impurities. After centrifugation, the upper 80% of supernatants were collected for the preparation of films. The CS/CNTs film was prepared by casting this solution at room temperature for 12 h. The CS/CNTs film was immersed in a dilute ammonia/methanol solution for 2 h to neutralize the acid and then in 70% ethanol for 12 h. Hereafter, CS/CNTs films with CNT concentrations of 1.3, 2.6, 3.8, 5.1, and 6.3 wt% are referred to as CS/CNTs (1.3), CS/CNTs (2.6), CS/CNTs (3.8), CS/CNTs (5.1), and CS/CNTs (6.3), respectively.

Surface characterization

Raman spectroscopy

Raman spectroscopy measurement is used to characterize CNTs materials. Raman measurements were performed on the samples in the wavenumber range from 1,200 to 2,000 cm^{-1} using a Raman spectrometer (LabRAM, Jobin-Yvon, France) equipped with a He–Ne ion laser (632.8 nm).

X-ray photoelectron spectroscopy measurements

X-ray photoelectron spectroscopy (XPS) measurement is able to analyze the surface chemical bonds of the outermost layers. The atomic compositions of the modified films were determined by XPS (JEOL, Japan) utilizing MgK (1,253.6 eV) radiation as an X-ray source at 10 kV and 10 mA. The binding energies for all spectra were referenced to the C1s signal at 285.0 eV. Spectral resolution for high-resolution spectra was carried out with the supplied software. The percentages of atomic compositions were calculated using the manufacturer-supplied software.

Contact angle measurements

The surface wettability was measured using a Contact Angle Meter (Kyowa Interface Science Co., Ltd.) equipped with a microliter syringe at room temperature. A distilled water droplet (1.0 μl) was dropped onto the sample surface. The average value of the contact angle was determined by measuring at five different positions on the same sample.

Atomic force microscope observation

Surface topography measurements were performed using an atomic force microscope (AFM; Nanoscope, Digital

Instruments). The measurement was performed using a tapping mode with a single crystal Si cantilever at a resonant frequency of about 130 kHz. Height images of 10-μm-square samples were taken at ambient temperature. The arithmetic mean of the surface average roughness (Ra) was estimated directly from AFM images. The Ra was calculated from three different areas on each surface and averaged.

Bovine aortic endothelial cells attachment

Bovine aortic endothelial cells (BAECs) were cultured in Dulbecco's modified Eagle medium (DMEM) (Nissui Pharmaceutical Co., Ltd., Tokyo, Japan) supplemented with 10% fetal bovine serum (Gibco, USA), 1% antibiotic/antimycotic solution (100 units penicillin, 100 μg streptomycin, and 0.25 μg amphotericin B; Sigma Aldrich). They were incubated in a humid atmosphere of 5% CO_2. The culture medium was changed every 2 days. Cells were routinely passed using a 0.5% trypsin-EDTA solution (Gibco, USA). Cultures of 80% confluent BAECs were used for all experiments. BAECs were subsequently seeded at a concentration of 1.0×10^4 cells/cm^2. The cells were then cultivated for 24 h in a humidity incubator (5% CO_2 at 37°C). The samples were gently washed twice with sterilized phosphate buffer saline (PBS) in order to remove any non-attached cells. Finally, the cell morphology was observed using a phase-contrast microscope (Olympus IX71 microscope).

In vitro platelet adhesion tests

Fresh human blood was mixed with 3.8% sodium citrate (1:9 ratio, v/v) and centrifuged at 110g for 15 min to obtain the platelet-rich plasma (PRP). After removing the PRP, the remains were further centrifuged at 2,000g for 15 min to obtain the platelet-poor plasma (PPP). The concentration of platelets in PRP was adjusted to 1.0×10^5 platelets/μl by dilution with PPP. Platelet suspension (100 μl) was placed onto the film surface and was incubated for 30 min at 37°C in a 5% CO_2 atmosphere. After incubation, the film surfaces were thoroughly rinsed with PBS twice to remove non-adhering platelets. The films were immersed in 2.5% glutaraldehyde in PBS for 2 h at 4°C to immobilize platelets on the film. The films were dehydrated in a series of ethanol/water solutions of increasing ethanol concentration (30, 50, 70, 90, and 100% v/v) for 15 min each. Platelet adhesion was evaluated with scanning electron microscopy (SEM) (SUPRA40, Carl Zeiss, Japan).

In vitro Ca^{2+} re-added platelet activation tests

PRP (1.0×10^5 platelets/μl) plasma was obtained from 3.8% sodium citrate solution-fresh human blood. Ca^{2+} replenished platelet adhesion experiments were performed. A total of 40 μl of $CaCl_2$ solution (0.5 mol/l) was added to 1.0 ml fresh PRP. Platelet suspension (100 μl) was placed onto the film surface and was incubated for 10 min at 37°C in a 5% CO_2 atmosphere. After incubation, the films were rinsed with PBS twice and then immersed in 2.5% glutaraldehyde solution for 2 h at 4°C. After the dehydrating treatment, platelet activation was observed using SEM.

Results

Raman spectroscopy

The Raman spectra of each composite film are shown in Fig. 2. Since the Raman intensity of chitosan film is small and seen in the vicinity of Raman shift 1,100 and 3,300, it is not shown in the range displayed in Fig. 2 (Raman shift 1,200–1,800 cm^{-1}). The peak intensities for CS/CNTs composite films appeared at 1,600 and 1,300 cm^{-1}, and were attributed to graphite structure (G band) and disordered graphite structure (D band) derived from structurally disrupted graphite sheets composing CNTs, respectively.

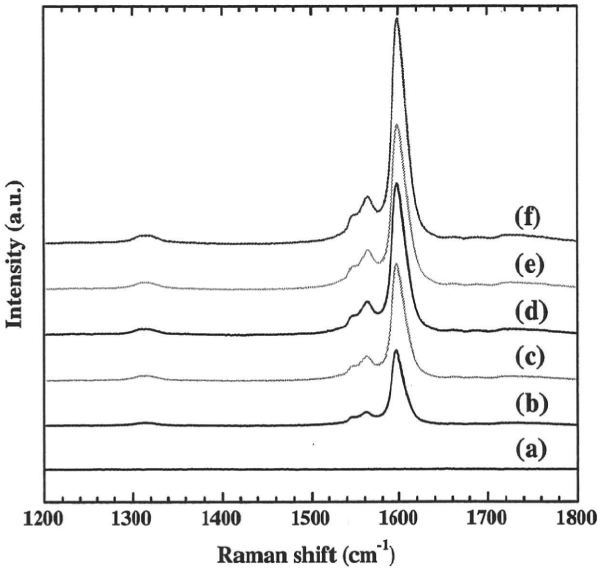

Fig. 2 Raman spectra of (a) CS film, (b) CS/CNTs (1.3), (c) CS/CNTs (2.6), (d) CS/CNTs (3.8), (e) CS/CNTs (5.1), and (f) CS/CNTs (6.3) composite films. The excitation wavelength is 632.8 nm

It is obvious that the intensity of each peak increased with each increment of added CNTs.

XPS analysis

The resolved C1s XPS spectra of the original chitosan film and the CS/CNTs composite film with various amounts of CNTs are presented in Fig. 3. The ratio of atomic composition and relative content of CNTs and carbon species are summarized in Table 1. As CNTs are composed of pure carbon, the addition of CNTs induced the increase in the atomic proportion of carbon and, conversely, the decrease in the proportions of oxygen and nitrogen. The C1s spectra of chitosan film were resolved into three peaks at approximately 285.0, 286.5, and 288.1 eV attributed to C–C/C–H, C–N/C–O/C–O-C, and C=O/O–C–O, respectively. The C1s spectra appearing at around 284.1 eV were attributed to the sp^2 bonds of CNTs structures. The peak at 284.1 eV was mainly assigned to CNTs and the peak intensity increased with increasing amounts of CNTs. The XPS results revealed that CNTs existed on the CS/CNTs films' surface layers.

AFM observation

AFM image of each sample surface is shown in Fig. 4. The chitosan film surface was relatively smooth, while the surface of the composite film was rugged, with the roughness between 30 and 50 nm which increased remarkably with the increment of CNTs. It is clear that the formation of microbulging on the surface of composite films was highly influenced by the amount of CNTs. The relationship between the values of Ra (surface roughness parameter) and concentrations of CNTs is listed in Table 2. The surface roughness increased with CNTs concentration. This result implies that the amount of CNTs greatly increased the proportion of carbon species and surface roughness of CS/CNTs composite film.

Contact angle measurements

The contact angles of all of the composite films were measured and are shown in Fig. 5. The contact angle of chitosan film is approximately 70.5 ± 3.7°. The contact angles were not significantly changed when the concentration of CNTs

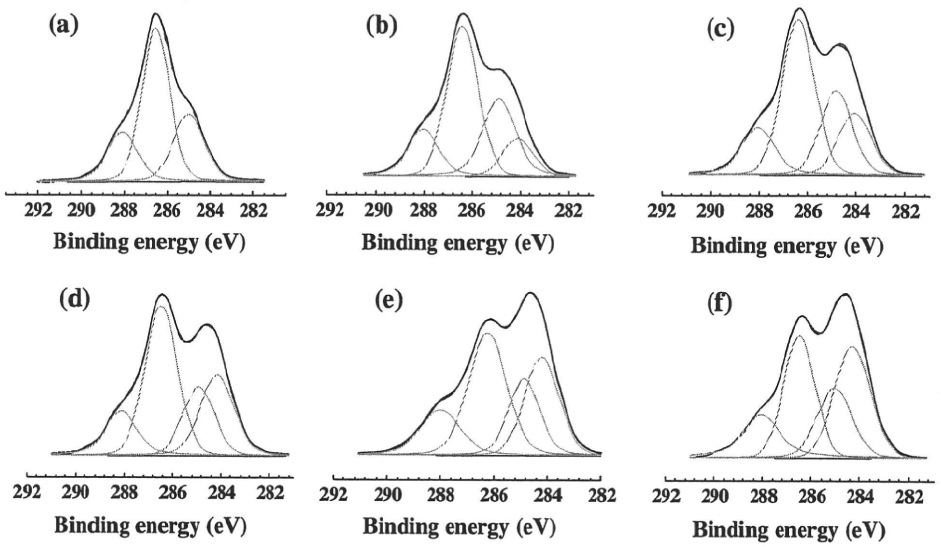

Fig. 3 Resolved C1s XPS spectra of (**a**) CS film, (**b**) CS/CNTs (1.3), (**c**) CS/CNTs (2.6), (**d**) CS/CNTs (3.8), (**e**) CS/CNTs (5.1), and (**f**) CS/CNTs (6.3), respectively. The peaks at 284.1, 285.0, 286.5, and 288.1 eV were attributed to carbon nanotubes C–C/C–H, C–O/C–N/C–O–C, and C=O/O–C–O, respectively

Table 1 Elemental ratios of carbon, oxygen, nitrogen, and the relative content comparison of different binding energies of carbon (C1s) species

Samples	Carbon	C1s (at%)				O1s (at%)	N1s (at%)
		284.1 eV Carbon nanotubes	285.0 eV C–C, C–H	286.5 eV C–O, C–N, C–O–C	288.0 eV C=O, O–C–O	Oxygen	Nitrogen
Original CS film	60.71	–	28.34	55.25	16.41	32.75	6.54
CS/CNTs (1.3)	63.96	11.44	25.70	48.40	14.50	29.88	6.17
CS/CNTs (2.6)	65.75	16.74	24.53	45.48	13.25	28.79	5.46
CS/CNTs (3.8)	66.84	22.17	20.35	45.75	11.73	28.80	4.36
CS/CNTs (5.1)	67.50	27.74	18.17	39.32	14.76	27.42	5.08
CS/CNTs (6.3)	71.75	33.72	21.07	32.15	13.05	23.80	4.45

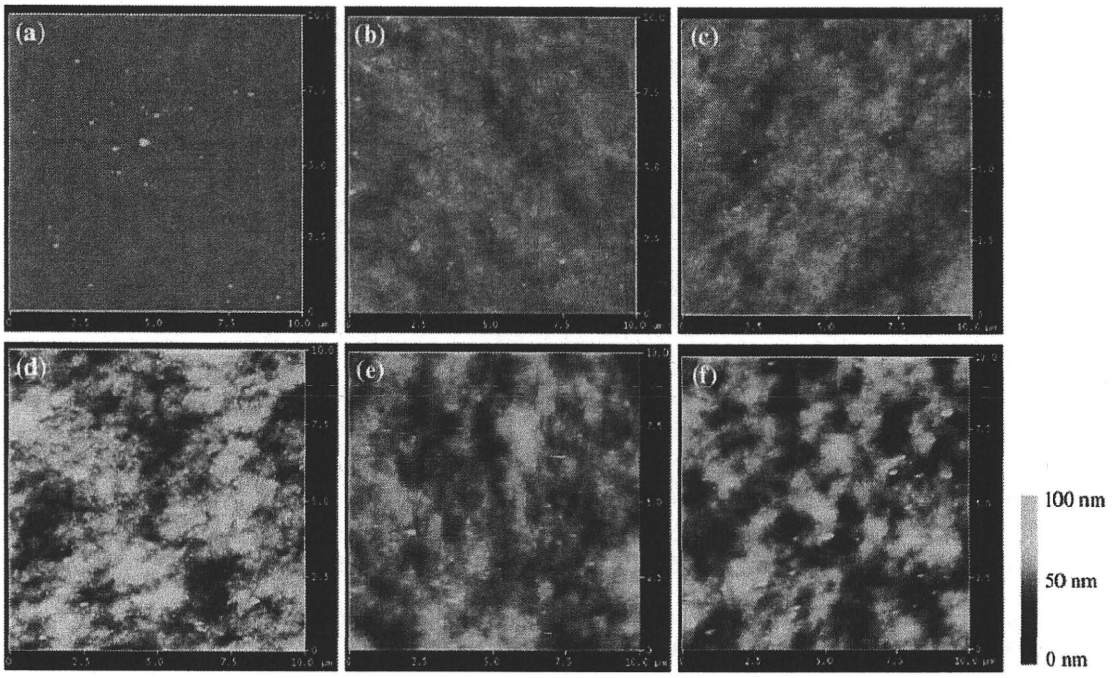

Fig. 4 AFM images of (**a**) CS film, (**b**) CS/CNTs (1.3), (**c**) CS/CNTs (2.6), (**d**) CS/CNTs (3.8), (**e**) CS/CNTs (5.1), and (**f**) CS/CNTs (6.3), respectively. The scan size is 10 × 10 μm

Table 2 Surface roughness (Ra) of the prepared samples

Samples	Surface roughness Ra (nm)
CS film	1.2 ± 0.01
CS/CNTs (1.3)	2.3 ± 0.19
CS/CNTs (2.6)	3.2 ± 0.13
CS/CNTs (3.8)	5.4 ± 0.18
CS/CNTs (5.1)	6.7 ± 0.54
CS/CNTs (6.3)	10.1 ± 0.76

The Ra value is the average surface roughness parameter

were between 0 and 2.6 wt%. However, the contact angles rose at the CNTs concentration of 3.8 wt% and gradually increased up to around 90° at the concentration of 6.3 wt%. CNTs are known to be extremely hydrophobic. This result confirmed that the concentration of CNTs higher than 3.8 wt% modified the surface so as to make it more hydrophobic.

BAECs attachment

The phase contrast micrographs of BAECs attachment after 24 h cultivation are presented in Fig. 6. It was clearly observed that the shapes of the BAECs are flat and are well spread with pseudopodia. It is suggested to be activated on CS/CNTs(3.8), CS/CNTs(5.1), and CS/CNTs(6.3). In contrast, BAECs grown on the chitosan film appeared to retain a spherical shape and only a small number of clusters

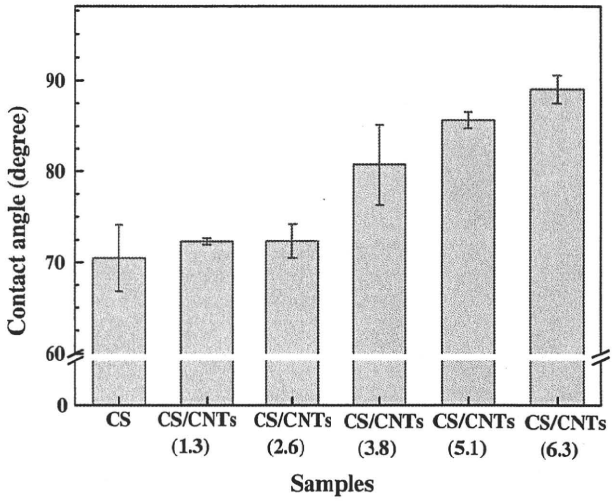

Fig. 5 Contact angles of CS film and CS/CNTs composite films

were demonstrated. It is well known that the formation of pseudopodia is a sign that a cell is successfully anchored on the scaffold. Furthermore, whiteness and a spherical shape often indicate incipient cell death [11]. Hence, the BAECs interact with the surface of CS/CNTs composite film. Figure 7 displays the number of BAECs attached to each composite film. There was a significant difference in the cell number between chitosan and CS/CNTs composite films. Consequently, these results suggest that CNTs appearing on the surface of the composite film must play an important role in enhancing BAECs attachments.

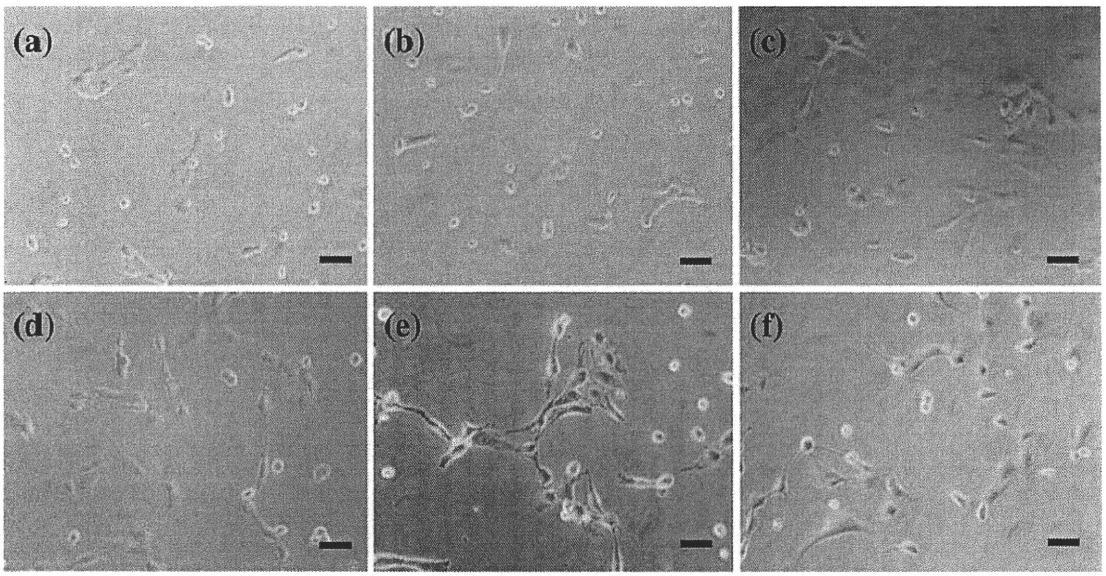

Fig. 6 Phase contrast micrographs of BAECs attached onto (**a**) CS film, (**b**) CS/CNTs (1.3), (**c**) CS/CNTs (2.6), (**d**) CS/CNTs (3.8), (**e**) CS/CNTs (5.1), and (**f**) CS/CNTs (6.3) after 24 h cultivation at 37°C, 5% CO_2 atmosphere (scale bar: 100 μm)

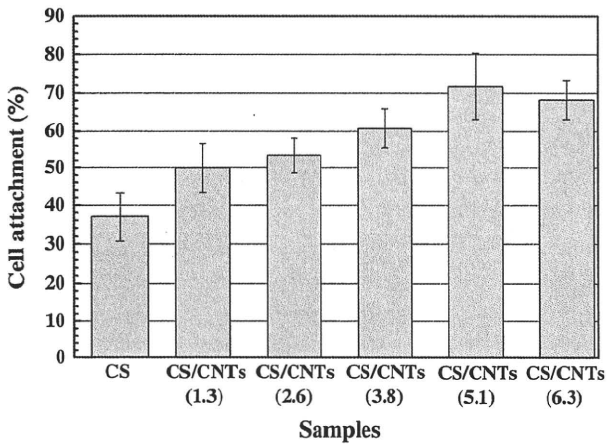

Fig. 7 The percentages of BAECs attachment on each sample after 24 h cultivation

In vitro platelet adhesion

The SEM images of platelets adhering onto the surfaces of composite films are presented in Fig. 8. Chitosan film showed a striking promotion of platelet adhesion and aggregation. The platelets were fully spread and formed focal clumps. The adhesion and activation of platelets on CS/CNTs composite films (concentration: 5.1 and 6.3 wt%) were greatly inhibited. The adhered platelets displayed a spherical morphology and the formation of pseudopodia was not demonstrated. The results indicated that CNTs on the surface of the composite film induced minimum platelet activation.

Ca^{2+}-replenished platelet adhesion test

Figure 9 shows an in vitro platelet adhesion test using Ca^{2+} for 10 min. Fully activated platelets connected with the fibrin network were observed on the chitosan film. This tendency was still observed at the concentration of CNTs of 3.8 wt%. However, platelet activation and subsequent fibrin network formation were completely inhibited on the surface of CS/CNTs composite films with CNTs concentrations of 5.1 and 6.3. These results indicate that a high concentration of CNTs satisfactorily inhibited the activation of platelets.

Discussion

The surface analyses of CS/CNTs composite film revealed that the concentration of CNTs on the composite film surface increased with increasing amounts of CNTs. Moreover, the surface properties, such as topography and wettability, were greatly affected at higher CNTs concentration, i.e., more than 3.8 wt%. BAECs attachment tests indicated that the cell attachment property was improved on CS/CNTs composite film compared to that of chitosan film. This result is supported by a previous study by Smart et al. [12]. They reported that CNTs demonstrated excellent biocompatibility with good adherence of endothelial cells. Platelet adhesion tests demonstrated that platelet adhesion and aggregation were depressed by CNTs compositions with concentrations higher than 3.8 wt%. Our results were consistent with some studies for the blood compatibility of

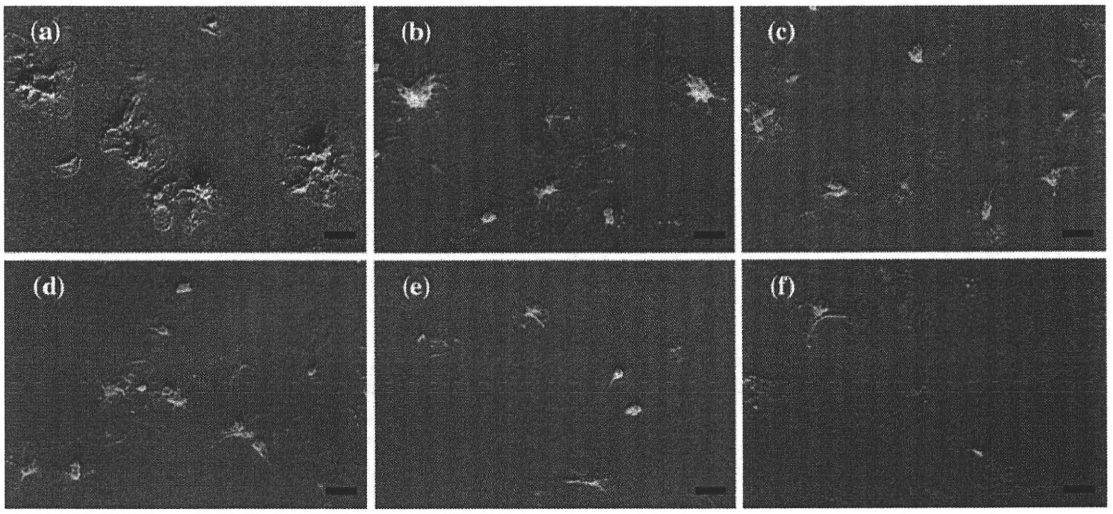

Fig. 8 SEM images of platelet adhesion on (**a**) CS film, (**b**) CS/CNTs (1.3), (**c**) CS/CNTs (2.6), (**d**) CS/CNTs (3.8), (**e**) CS/CNTs (5.1), and (**f**) CS/CNTs (6.3) after incubation of 30 min at 37°C, 5% CO_2 atmosphere (scale bar: 5 μm)

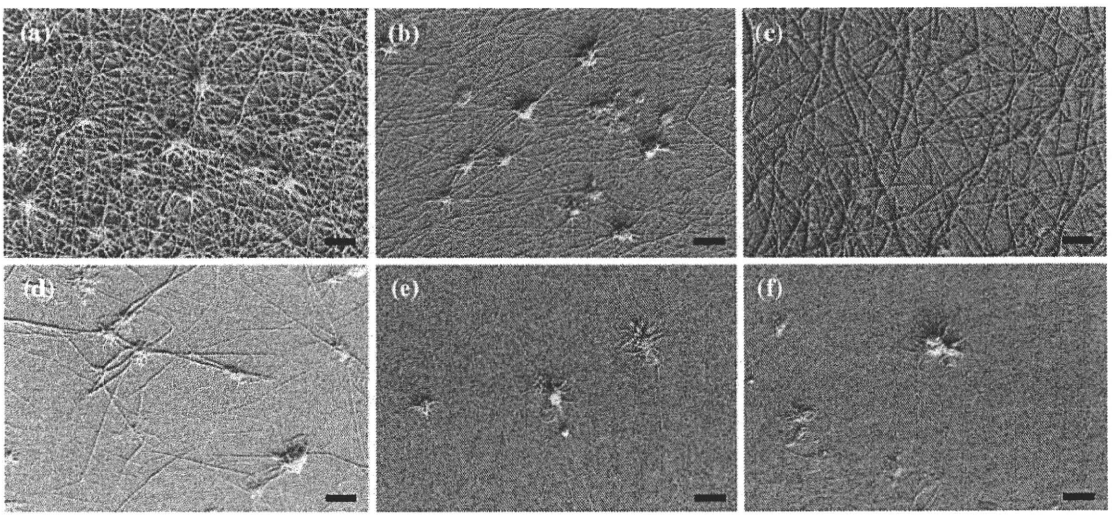

Fig. 9 SEM images of Ca^{2+} re-added platelet adhesion on (**a**) CS film, (**b**) CS/CNTs (1.3), (**c**) CS/CNTs (2.6), (**d**) CS/CNTs (3.8), (**e**) CS/CNTs (5.1), and (**f**) CS/CNTs (6.3) after 10 min incubation at 37°C, 5% CO_2 atmosphere (scale bar: 5 μm)

CNTs materials [13]. Meng et al. [8] reported that a polyurethane multi-walled carbon nanotubes composite surface displayed a significantly improved anticoagulant function. In our experiment, it was confirmed again that the amount of CNTs on the film surface significantly inhibited the activation of platelet function. Furthermore, the results of the Ca^{2+} platelet activation test revealed that the formation of a fibrin network following platelet aggregation was minimized by increasing CNTs concentration. The surfaces of CS/CNTs (CNTs concentration: 5.1 and 6.3) composite films did not only have an antithrombogenic property, but they also retain easy adherence of endothelial cells. The novel composite film of CS/CNTs (CNTs concentration: 5.1 and 6.3) that we developed offers the ideal antithrombogenetic membrane for application to the surface of artificial blood vessels. At present, polyester fiber is being used for artificial blood vessels. Several studies have reported that chitosan possesses the ability to adhere to the polyester fiber with some modification [14–16]. Thus, the CS/CNTs composite films would be high-potential candidates for artificial blood vessel coating materials. Future studies focusing on biological examination as the implants material will be necessary.

In summary, our work presents the investigation of the surface characterization of CS/CNTs composite films and their blood compatibility. We found that the cell

attachment property was enhanced on CS/CNTs composite films. Furthermore, platelet adhesion and platelet activation were remarkably inhibited on CS/CNTs composite films. We conclude that platelet adhesion and endothelial cell attachment can be controlled by the concentration of CNTs. It is expected that CS/CNTs composite films would be a promising coating material for implants in contact with blood, such as artificial vessels and endovascular stents.

References

1. Khor E, Lim LY. Implantable applications of chitin and chitosan. Biomaterials. 2003;24:2339–49.
2. Madihally SV, Matthew HW. Porous chitosan scaffolds for tissue engineering. Biomaterials. 1999;20:1133–42.
3. Zhu A, Zhang M, Wu J, Shen J. Covalent immobilization of chitosan/heparin complex with a photosensitive hetero-bifunctional crosslinking reagent on PLA surface. Biomaterials. 2002;23:4657–65.
4. Chou TC, Fu E, Wu CJ, Yeh JH. Chitosan enhances platelet adhesion and aggregation. Biochem Biophys Res Commun. 2003;302:480–3.
5. Chandy T, Sharma CP. Prostaglandin E_1-immobilized poly(vinyl alcohol)-blended chitosan membranes: blood compatibility and permeability properties. J Appl Polym Sci. 1992;44:2145–56.
6. Shim M, Kam NWS, Chen RJ, Li YM, Dai HJ. Functionalization of carbon nanotubes for biocompatibility and biomolecular recognition. Nano Lett. 2002;2:285–8.
7. Mattson MP, Haddon RC, Rao AM. Molecular functionalization of carbon nanotubes and use as substrates for neuronal growth. J Mol Neurosci. 2000;14:175–82.
8. Meng J, Kong H, Xu HY, Song L, Wang CY, Xie SS. Improving the blood compatibility of polyurethane using carbon nanotubes as fillers and its implications to cardiovascular surgery. J Biomed Mater Res A. 2005;74:208–14.
9. Dhand C, Arya SK, Datta M, Malhotra BD. Polyaniline–carbon nanotube composite film for cholesterol biosensor. Anal Biochem. 2008;383:194–9.
10. Takahashi T, Luculescu CR, Uchida K, Ishii T, Yajima H. Dispersion behavior and spectroscopic properties of single-walled carbon nanotubes in chitosan acidic aqueous solutions. Chem Lett. 2005;34:1516–7.
11. Thom VH, Altankov G, Groth Th, Jankova K, Jonsson G, Ulbricht M. Optimizing cell–surface interactions by photografting of poly(ethylene glycol). Langmuir. 2000;16:2756–65.
12. Smart SK, Cassady AI, Lu GQ, Martin DJ. The biocompatibility of carbon nanotubes. Carbon. 2006;44:1034–47.
13. Koh LB, Rodriguez I, Zhou J. Platelet adhesion studies on nanostructured poly(lactic-co-glycolic-acid)-carbon nanotube composite. J Biomed Mater Res A. 2008;86:394–401.
14. Rémy M, Valli N, Brethes D, Labrugère C, Porté-Durrieu MC, Dobrova NB, Novikova SP, Gorodkov AJ, Bordenave L. In vitro and in situ intercellular adhesion molecule-1 (ICAM-1) expression by endothelial cells lining a polyester fabric. Biomaterials. 1999;20:241–51.
15. Jou CH, Yuan L, Lin SM, Hwang MC, Chou WL, Yu DG, Yang MC. Biocompatibility and antibacterial activity of chitosan and hyaluronic acid immobilized polyester fibers. J Appl Polym Sci. 2007;104:220–5.
16. Correlo VM, Boesel LF, Bhattacharya M, Mano JF, Neves NM, Reis RL. Hydroxyapatite reinforced chitosan and polyester blends for biomedical applications. Macromol Mater Eng. 2005;290:1157–65.

Sensors and Materials, Vol. 21, No. 7 (2009) 385–391
MYU Tokyo

S & M 0778

High-Temperature Operation of Single-Electron Transistors Based on Single-Walled Carbon Nanotubes

Takahiro Mori[1,*], Shunsuke Sato[1,2], Kazuo Omura[1,3], Shota Yajima[1,3], Yasuhiro Tsuruoka[4], Katsumi Uchida[3], Yohji Achiba[4], Hirofumi Yajima[3] and Koji Ishibashi[1]

[1]Advanced Device Laboratory, RIKEN (The Institute of Physical and Chemical Research), 2-1 Hirosawa, Wako, Saitama 351-0198, Japan
[2]Department of Physics, Tokyo University of Science, 1-3 Kagurazaka, Shinjuku-ku, Tokyo 162-8601, Japan
[3]Department of Applied Chemistry, Tokyo University of Science, 1-3 Kagurazaka, Shinjuku-ku, Tokyo 162-8601, Japan
[4]Department of Chemistry, Tokyo Metropolitan University, 1-1 Minami-Osawa, Hachioji, Tokyo 192-0397, Japan

(Received February 28, 2009; accepted June 1, 2009)

Key words: carbon nanotube, single-electron transistor, ion irradiation, surfactant

Single-electron transistors (SETs) are one of the possible devices for use as transducers for highly sensitive sensors that can detect small charges. We describe two approaches to fabricating high-temperature-operable single-walled carbon nanotube (SWCNT) SETs, which can operate above the temperature of liquid nitrogen, with a mass-production-adaptable process. One approach involves a SET with SWCNTs dispersed in a carboxymethylcellulose (CMC)/water suspension, which can improve the SWCNT/metal interface properties by increasing the barrier height, so that Coulomb oscillations can be observed up to 80 K. The other approach involves a SET with a segmented Coulomb island between two higher resistance parts in an individual SWCNT, which were induced by Ar ion irradiation. This SET has been operated at up to 100 K, and the operation temperature could be increased by the improvement in the device structure.

*Corresponding author: e-mail: tmori@riken.jp

1. Introduction

The detection of small charges is one of the key issues in achieving higher sensitivity of sensors such as biosensors. Now, nanomaterial-based field-effect transistors (FETs) are widely used to improve the sensitivity of biosensors[1,2] by improving the transconductance of FETs. Considering the detection of small charges, we can easily speculate on the great potential of single-electron transistors (SETs) as transducers of future sensors. SETs operate with a current of single-electron order on the basis of the Coulomb blockade effect.[3] Thus, SETs are also promising candidates for use as fundamental components that can act as an alternative to FETs for future electronics, because of the expectation of their use in low-power-consumption technologies.[4]

To improve the performance of SETs, single-walled carbon nanotubes (SWCNTs) are one of the natural choices as a building block of SETs because of their extremely small structure with diameters of ~1 nm.[3] An important issue in the SET research field is the operation temperature, because it is difficult to achieve room-temperature (RT) operation of SETs. There are two device parameters that determine the operation temperature, one is the charging energy for a single electron $E_C = e^2/C_\Sigma$, where C_Σ is the self-capacitance of the Coulomb island, and the other is the tunnel barrier height φ_B to confine electrons in the island. The simplest device structure of a SWCNT-SET contains two metallic contacts (source and drain contacts) deposited on an individual SWCNT and the SWCNT between the contacts forms a Coulomb island, where tunnel barriers are formed at the SWCNT/metal interfaces.[3] This device operates up to approximately 20 K, with typical values of the parameters, which are an E_C of 10–20 meV and a φ_B of about 10 meV.[5] In this device, the self-capacitance C_Σ, which is the sum of the gate capacitance and the barrier capacitances, is dominated by the barrier capacitances. Here, we can easily determine that the barrier properties play an important role in achieving the RT operation of the SWCNT-SET. By determining how to form the barriers, RT operations of the SWCNT-SET have been achieved and are reported in some papers.[6,7]

In this paper, we describe two approaches to improving the temperature characteristics of the SWCNT-SET. One approach involves the modification of the SWCNT/metal interface barriers using the simplest device structure mentioned above. The effect of the adsorbed molecules or atoms on the properties of the SWCNT/metal interface has been mentioned in some papers.[8–10] In the fabrication process of the SWCNT-SET by the dispersion method, we must use a dispersant to obtain individual SWCNTs, and adsorbed dispersants affect the SWCNT/metal interface properties. Carboxymethylcellulose (CMC) is our choice as a dispersant, and it modified the interface properties to obtain a higher φ_B of approximately 20 meV, which resulted in an operation temperature of the finished SWCNT-SETs of up to 80 K. The other approach involves barrier formation by low-energy Ar ion irradiation. Individual SWCNTs were partly irradiated through the two openings to induce two higher resistance parts. The irradiated parts act as the tunnel barriers and the segment between the irradiated parts forms the Coulomb island. We demonstrate SET operation up to 100 K in this study, but the operation temperature could increase with modification of the device structure.

2. Dispersant Effect on Barrier Height

To fabricate SWCNT-SETs by the dispersion method, surfactants such as Triton X-100 or sodium dodecylsulfate (SDS) are commonly used as a dispersant to produce an SWCNT suspension in which individual SWCNTs are dispersed. The SWCNT-SET with the simplest device structure, fabricated with a Triton X-100/water suspension was operated up to 20 K as previously reported.[5] CMC is a polymer, a derivative of cellulose. It can work as a dispersant similarly to surfactants, as described in ref. 11. In both cases we used the simplest device structure of the SWCNT-SETs with a back gate. The details of the device fabrication process are given in ref. 12.

The differential conductance mapping of the SWCNT-SET fabricated with the CMC/water suspension is shown in Fig. 1. The series of white diamond shapes are so-called Coulomb diamonds with no flowing current, which are a standard feature of the SET. The lines outside the diamonds indicate the effect of the zero-dimensional confined state, which means that the Coulomb island is a quantum dot. The roughly estimated device parameters from the diamonds are a charging energy of 8 meV, an energy splitting of the zero-dimensional states ΔE of 2 meV, and a C_G/C_Σ ratio of 0.1. The C_G/C_Σ ratio indicates that the barrier capacitances are dominant in the C_Σ.

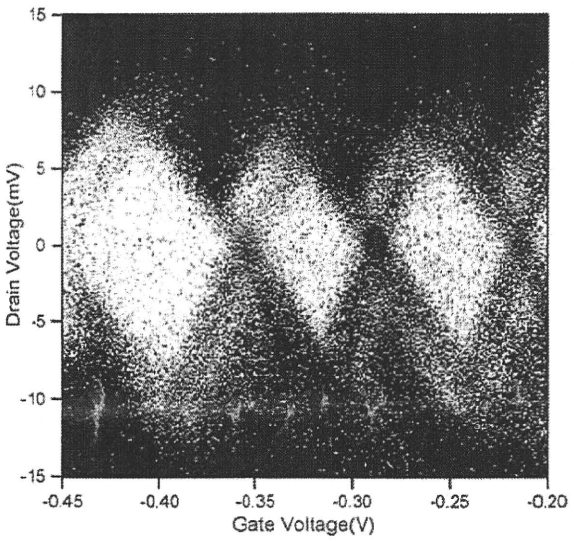

Fig. 1. Differential conductance mapping as a function of the drain and gate voltages. The measurement temperature was 1.5 K. The white areas indicate zero conductance. Coulomb diamonds can be clearly observed with the zero-dimensional confined state lines.

The temperature dependence of the Coulomb oscillations is shown in Fig. 2. Regular Coulomb oscillations were observed up to 80 K, which means that the SET operates as high as 80 K. This operation temperature was much higher than that of the SET fabricated with the Triton X-100/water suspension; however, there is no notable difference in the charging energy between these two devices. The factor that determines the operation temperature difference is φ_B. The φ_B of the SET fabricated with the Triton X-100/water suspension was typically less than 10 meV, in contrast to the φ_B of approximately 20 meV of the SET fabricated with the CMC/water suspension, as estimated from Fig. 3.

The improvement in the temperature characteristics resulted from the dispersant difference, which suggests that adsorbed dispersant molecules on the SWCNT modify the SWCNT/metal interface properties. We can easily speculate that the molecule-induced dipoles change the surface potential of the contact metal at semiconductor/metal interfaces with the adsorbed organic molecules at the interface.[13,14]

3. Barrier Formation with Ar Ion Irradiation Technique

A schematic of the induction of Ar-ion-irradiated parts in an individual SWCNT is shown in Fig. 4. An individual SWCNT with two electrodes was covered with a protection resist and two openings for Ar ion irradiation were fabricated by electron beam lithography. The protected regions of the SWCNT had no defects induced by the Ar ion irradiation, but the opened regions exhibited induced defects and had higher resistance than the protected regions. In this paper, we describe the results achieved with a device in which the gap between electrodes was about 1 μm, the width of the openings was about 50 nm, and the gap between the openings was about 300 nm. The details of the fabrication procedure are given in ref. 15.

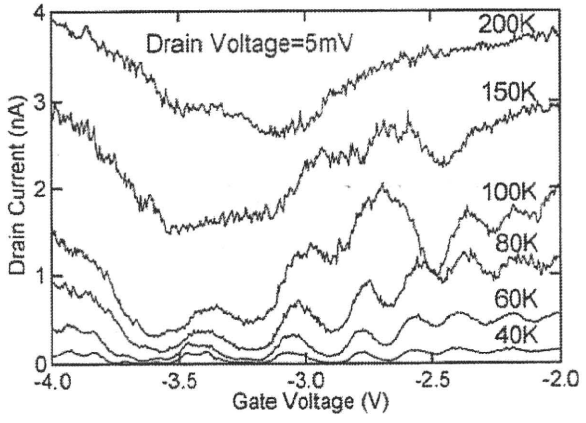

Fig. 2. Gate characteristics at 40–200 K. Coulomb oscillations can be clearly observed up to 80 K.

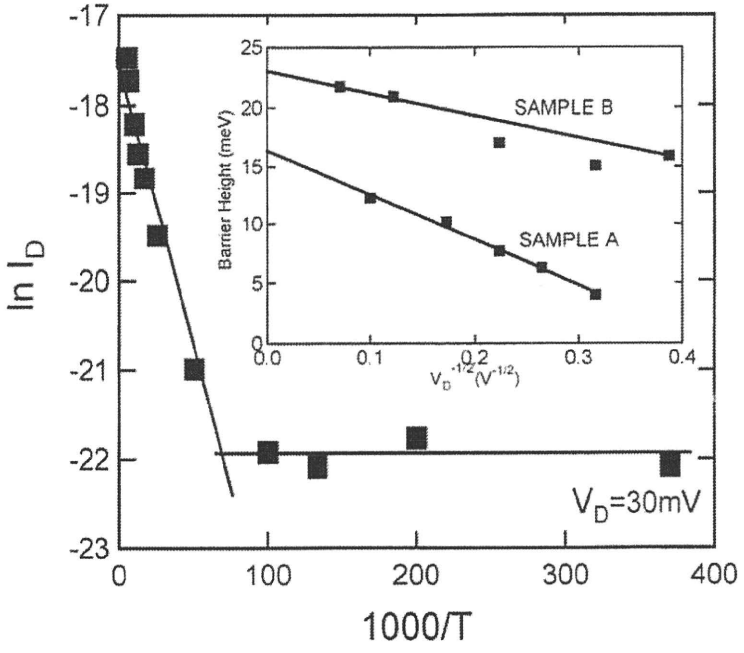

Fig. 3. Temperature dependence of the drain current with 30 mV of drain voltage. The barrier height was estimated from the slope of the high-temperature side of the plot. The inset shows the drain voltage dependence of the barrier height.

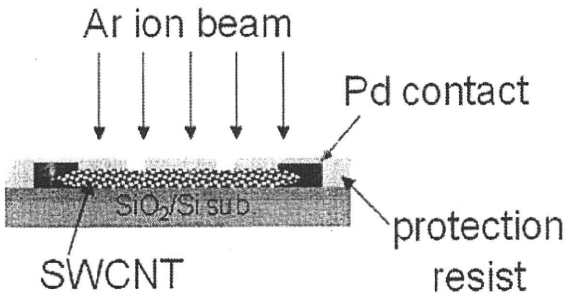

Fig. 4. Schematic cross-sectional image of the Ar-ion-irradiation process. The device was covered with protection resist and two openings were fabricated by electron beam lithography.

The SETs fabricated by this method were successfully operated, and the temperature dependence of the Coulomb oscillations is shown in Fig. 5. Regular Coulomb oscillations were observed up to 100 K, with a drain voltage of 30 mV. The barriers were successfully formed by low-energy Ar ion irradiation. In our device formation process, we should consider the electron irradiation effect on SWCNTs, as reported in ref. 16, because we used electron lithography to form the openings. However, no notable changes in the device properties were observed, such as a reduction in resistance or gate modulation. This may be because of a discrepancy in the electron absorption efficiency caused by the difference in electron acceleration voltages used in the experiments.

The notable feature of this device was the small barrier capacitance. The estimated sum of the two barrier capacitances was about 0.8 aF, and the gate capacitance dominated the total capacitance. Thus, we can expect much higher SET operation with the reduction in the gate capacitance, which can be achieved with the reduction in the Coulomb island size determined by electron beam lithography.

4. Summary

We described two approaches to fabricate SWCNT-SETs that can operate at higher temperatures. One involves barrier height modification using the polymer dispersant, carboxymethylcellulose. The fabricated SET operated up to 80 K with a barrier height of about 20 meV. The other involves barrier formation using Ar ion irradiation. The fabricated SET operated up to 100 K with small barrier capacitances of about 0.4 aF.

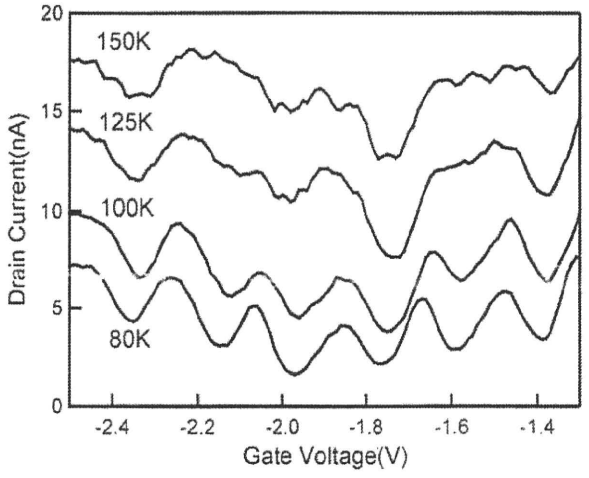

Fig. 5. Gate characteristics at 80–150 K with a drain voltage of 30 mV. Coulomb oscillations can be observed up to 100 K.

Acknowledgement

This work was partially supported by a KAKENHI, Grant-in-Aid for Young Scientists, No. 200710110, from MEXT.

References

1 G. Zheng, F. Patolsky, Y. Cui, W. U. Wang and C. M. Lieber: Nat. Biotechnol. **23** (2005) 1294.
2 K. Maehashi, T. Katsura, K. Kerman, Y. Takamura, K. Matsumoto and E. Tamiya: Anal. Chem. **79** (2007) 782.
3 K. Ishibashi, S. Moriyama and T. Fuse: IEICE Trans. Electron. **E87-C** (2004) 1799.
4 International Technology Roadmap for Semiconductors: http://www.itrs.net/.
5 D. Tsuya, M. Suzuki, Y. Aoyagi and K. Ishibashi: Jpn. J. Appl. Phys., Part 1 **44** (2005) 1588.
6 H. Postma, T. Teppen, Z. Yao, M. Grifoni and C. Dekker: Science **293** (2001) 76.
7 K. Maehashi, H. Ozaki, Y. Ohno, K. Inoue, K. Matsumoto, S. Seki and S. Tagawa: Appl. Phys. Lett. **90** (2007) 023103.
8 S. Heinze, J. Tersoff, R. Martel, V. Derycke, J. Appenzeller and Ph. Avouris: Phys. Rev. Lett. **89** (2002) 106801.
9 X. Cui, M. Freitag, R. Martel, L. Brus and P. Avouris: Nano. Lett. **3** (2003) 783.
10 J. Li, Q. Zhang, H. Li and M. B. Chan-Park: Nanotechnology **17** (2006) 668.
11 T. Takahashi, K. Tsunoda, H. Yajima and T. Ishii: Jpn. J. Appl. Phys., Part 1 **43** (2004) 3636.
12 T. Mori, K. Omura, S. Sato, M. Suzuki, K. Uchida, H. Yajima and K. Ishibashi: Appl. Phys. Lett. **91** (2007) 263511.
13 R. T. Tung: Phys. Rev. B **64** (2001) 205310.
14 H. Ishii, K. Sugiyama, E. Ito and K. Seki: Adv. Mater. (Weinheim, Ger.) **11** (1999) 605.
15 T. Mori, S. Sato, K. Omura, S. Yajima, Y. Tsuruoka, Y. Achiba and K. Ishibashi: J. Vac. Sci. Technol., B (in press).
16 T. Suzuki and Y. Kobayashi: Jpn. J. Appl. Phys., Part 2 **44** (2005) L1498.

Toxicology 261 (2009) 19–24

Contents lists available at ScienceDirect

Toxicology

journal homepage: www.elsevier.com/locate/toxicol

Attenuation of delayed-type hypersensitivity by fullerene treatment

Keichiro Yamashita[a], Masanobu Sakai[a], Naoya Takemoto[a], Mitsutoshi Tsukimoto[a], Katsumi Uchida[b], **Hirofumi Yajima[b]**, Shigeru Oshio[c], Ken Takeda[a], Shuji Kojima[a,*]

[a] Faculty of Pharmaceutical Sciences, Tokyo University of Science (TUS), 2641 Yamazaki, Noda-shi, Chiba 278-8510, Japan
[b] Department of Applied Chemistry, Tokyo University of Science (TUS), 12-1 Funagawara, Shinjuku-ku, Tokyo 162-0826, Japan
[c] Faculty of Pharmaceutical Sciences, Ohu University, 31-1 Misumidou, Tomita-machi, Koriyama-shi, Fukushima, 963-8611, Japan

ARTICLE INFO

Article history:
Received 12 March 2009
Received in revised form 6 April 2009
Accepted 6 April 2009
Available online 17 April 2009

Keywords:
Nano-fullerene (nano-C_{60})
Attenuation
Delayed-type hypersensitivity (DTH)

ABSTRACT

Expansion and commercialization of nanotechnology mean that it is important to understand the potential health hazards of manufactured nanoparticles. Here, we focused on the effect of fullerene, a type of nanoparticle already in commercial use, on delayed-type hypersensitivity (DTH) induced by methyl-bovine serum albumin (mBSA). Delayed-type hypersensitivity was induced with methyl-bovine serum albumin in female C57BL/6 mice. A colloidal suspension of crystalline C_{60} (nano-C_{60}; average particle size 165 nm; 200 μL; 5.5 μg/mL) was injected intravenously twice, just before immunization and challenge with mBSA.

Nano-C_{60} treatment significantly attenuated footpad swelling, compared with that in DTH-disease control mice. Cytokine analysis indicated that nano-C_{60} treatment switched the cytokine balance towards Th1-dominance. Pro-inflammatory cytokines IL-6 and IL-17 were significantly increased in DTH mice, and these increases were significantly suppressed by nano-C_{60} treatment. Suppression of IL-17 by nano-C_{60} was confirmed in an *in vitro* splenocyte culture. However, production of TNF-α was increased in DTH mice, and the increase was significantly enhanced by nano-C_{60} treatment. The ratio of regulatory T (Treg) cells to total T ($CD4^+$) cells was also significantly increased by nano-C_{60} treatment, compared with that in DTH-disease control mice.

Nano-C_{60} treatment showed significant immunomodulatory effects in a mouse DTH model: IL-6 and IL-17 production was down-regulated, and the Treg cell ratio was up-regulated, concomitantly with attenuation of the pathology of DTH.

© 2009 Published by Elsevier Ireland Ltd.

1. Introduction

Nanoparticles often exhibit new or enhanced size-dependent properties compared with larger particles of the same material, and are expected to have practical applications in electronics, environmental science, medical science and many other fields (Emerich and Thanos, 2003; Moghimi et al., 2005; Satoh and Takayanagi, 2006). However, there is a risk of internal pollution with manufactured nanoparticles (Brown et al., 2001; Oberdörster et al., 2005). Since the diameter of nanoparticles is very small, their surface area is extremely large, and they may be much more toxic than larger particles. Furthermore, nanoparticles that enter the respiratory system may be distributed to the whole body via blood. It has been reported that diesel exhaust particles (DEP), which are nanoparticles often used as a model air pollutant, exert adjuvant effects on the response of humans and mice to inhaled or instilled allergens through the generation of oxidative stress (Ichinose et al., 1995; Diaz-Sanchez, 1997; Diaz-Sanchez et al., 1997; Fujimaki et al., 1997; Takano et al., 1997; Haley and Drazen, 1998). However, in general, little is known about the immunomodulatory effects of nanoparticles, or the mechanisms involved. Given the widespread potential applications of nanoparticles and their impending commercialization, human and environmental exposure to nanoparticles is likely to increase markedly in the near future. Therefore, early evaluation of the health effects of nanoparticles is important.

Fullerenes are a family of carbon allotropes composed entirely of carbon, in the form of hollow spheres, ellipsoids, tubes, or planar structures. The existence of carbon molecular structures was predicted by Osawa (1970), and fullerene (buckminsterfullerene; IUPAC name, C_{60}-I_h) was subsequently discovered in 1985 (Kroto et al., 1985). The structure of C_{60} resembles a soccer ball composed of twenty hexagons and twelve pentagons, and atoms composing the pentagons are more reactive than those composing the hexagons because of strain energy. The van der Waals diameter of a C_{60} molecule is about 1 nanometer (nm), and the nucleus-to-nucleus distance is about 0.7 nm. Fullerene has unique properties, and is expected to have practical applications in various fields (Da Ros and Prato, 1999; Tagmatarchis and Shinohara, 2001; Bosi et al.,

* Corresponding author. Tel.: +81 4 7121 3613; fax: +81 4 7121 3613.
E-mail address: kjma@rs.noda.tus.a.cjp (S. Kojima).

0300-483X/$ - see front matter © 2009 Published by Elsevier Ireland Ltd.
doi:10.1016/j.tox.2009.04.034

2003). Because of its radical scavenging activity, fullerene has been introduced as a component of cosmetics, which are now commercially available. Golf clubs, rackets, etc., that contain fullerene are also available. Thus, large-scale industrial production of fullerene has begun for a diverse and growing range of commercial applications within the last few years. Another biologically important property of C_{60} is the ability to form a long-lived triplet excited state upon photosensitization, so that it has the potential to generate singlet oxygen ($^1O_2$), a highly reactive form of molecular oxygen (Guldi and Prato, 2000). Singlet oxygen reacts with a wide variety of biological targets including lipids, proteins, nucleic acids and carbohydrates, and is known to be involved in cellular signaling and in cell damage (Briviba et al., 1997). In 2004, Oberdörster reported that C_{60} aggregates, prepared using a solvent extraction methodology, elevated lipid peroxidation levels and glutathione production in the brain and liver of largemouth fish (Oberdörster, 2004). Later, Sayes et al. (2005) reported increased lipid peroxidation and total glutathione in human cultured cells exposed to C_{60}. We speculated that fullerene might exert adjuvant effects on the response of mice sensitized with allergens through the generation of oxidative stress, like DEP. An understanding of the toxicity of fullerene is important for defining and constraining its possible biomedical applications.

Delayed-type hypersensitivity (DTH) is classified as type IV hypersensitivity, and is not antibody-dependent, but rather is a cell-mediated immunity involving antigen-specific effector Th1 and Th17 cells (Black, 1999; Särnstrand et al., 1999; Kobayashi et al., 2001). DTH reactions can be classically subdivided into tuberculin-type, Jones–Mote type and contact hypersensitivity. The tuberculin-type reaction was assayed in this study as a typical DTH reaction. DTH develops in two phases: in the sensitization phase, T cells are sensitized and antigen-specific effector Th1 and Th17 cells are formed. Next, in the elicitation phase, recall responses of these T cells are induced upon secondary challenge with the antigen. These effector T cells release cytokines, including IFN-γ and IL-17, that trigger recruitment of inflammatory cells such as neutrophils and macrophages (Nakae et al., 2002; Kariyone et al., 2003). The inflammation generally reaches a maximum at 24–48 h after secondary challenge.

In this study, we show that fullerene has an immunomodulatory action in a delayed-type hypersensitivity model in C57BL/6 mice. The mechanisms involved were examined, focusing on changes in inflammatory cytokines and Th17 cells, as well as regulatory T cells (Treg), which have a critical function in the regulation of autoimmune diseases, including DTH (Fontenot et al., 2003; Sakaguchi, 2004; Sato et al., 2006).

2. Materials and methods

2.1. Preparation of colloidal fullerene (nano-C_{60})

C_{60} was suspended in water according to the method of Deguchi et al. (2001), as follows. C_{60} (99.5%, Aldrich) was dissolved in tetrahydrofuran (THF) (Fisher Scientific) at a concentration of 100 mg/L. This solution was sparged with nitrogen and stirred overnight in the dark, then filtered through a 0.22 μm nylon filter (Osmonics, Fisher Scientific). An equal volume of MilliQ water was added to the solution of C_{60} in THF at a rate of 1 L/min. The resulting solution was dialyzed to eliminate the THF using Seamless Cellulose Tubing (Sanko Junyaku Tokyo, Japan). The final solution was stored overnight and then filtered through a 0.22 μm nylon filter to yield a colloidal suspension of crystalline C_{60} in water, which we refer to as nano-C_{60}.

2.2. Characterization of nano-C_{60}

The particle size distribution of nano-C_{60} was evaluated by means of dynamic light-scattering measurements (DLS, NICOMP 380 ZLS). The UV–vis spectra of nano-C_{60} suspensions were scanned within the wavelength range of 200–550 nm using a UV–vis spectrophotometer U-1100 (Hitachi). All UV–vis measurements were carried out at 20 °C, being automatically corrected for the suspending water.

2.3. Animals

Female C57BL/6 mice were purchased from Sankyo Labo Service (Tokyo, Japan) and used at 5–6 weeks of age. They were housed in plastic cages with paper chip bedding and bred in rooms kept at a temperature of 23 ± 2 °C and a relative humidity of 55 ± 10% under a 12 h light–dark cycle. They were allowed free access to tap water and experimental normal diet, CE-2 (CLEA Co., Tokyo, Japan). They were treated and handled according to the Guide Principles for the Care and Use of Laboratory Animals of the Japanese Pharmacological Society and with the approval of Tokyo University of Science's Institutional Animal Care and Use Committee.

2.4. Induction and evaluation of DTH

DTH was induced by immunization with mBSA (Sigma, St. Louis, MO, USA). Briefly, mice were injected SC with 200 μL of 1.25 mg/mL mBSA emulsified with Complete Freund's Adjuvant (CFA) (Chondrex, Redmond, WA) (immunization). Seven days after immunization, they were injected SC into one footpad with 20 μL of 10 mg/mL mBSA in PBS (challenge). Animals were injected with an equal volume of PBS into another footpad as a control. Evaluation of the responses was performed as described elsewhere (Särnstrand et al., 1999; Yoshimoto et al., 2000). At the indicated times after challenge, footpad thickness was measured with a digital caliper (Mitutoyo, Tokyo, Japan). The magnitude of the DTH response was determined as follows: [footpad swelling (mm)] = [footpad thickness of mBSA-injected footpad (mm)] − [footpad thickness of PBS-injected footpad (mm)], [footpad swelling (%)] = {[footpad swelling (mm)]/[footpad thickness of PBS-injected footpad (mm)]} × 100. Footpad swelling (%) was calculated as a percentage of the mean value of the control group.

2.5. Dosing schedule of nano-C_{60}

Mice of the nano-C_{60} treated group were administered IV with 200 μL of 5.5 μg/mL nano-C_{60} twice, just before immunization and challenge with mBSA. The dose of nano-C_{60} was determined with reference to previous reports (Oberdörster, 2004; Sayes et al., 2005). Control groups received only 200 μL of PBS on the same schedule as the nano-C_{60} treated group.

2.6. Reagents

The following antibodies were used for cytokine assay: purified anti-mouse TNF-α mAb (1F3F3D4), biotin-conjugated anti-mouse TNF-α mAb (MP6-XT22), purified anti-mouse IFN-γ mAb (XMG1.2), biotin-conjugated anti-mouse IFN-γ mAb (R4-6A2), purified anti-mouse IL-6 mAb (MP5-20F3), biotin-conjugated anti-mouse IL-6 mAb (MP5-32C11), purified anti-mouse IL-4 mAb (11B11), biotin-conjugated anti-mouse IL-4 mAb (BVD6-24G2) (eBioscience, San Diego, CA). Recombinant mouse TNF-α, IFN-γ, IL-4 and IL-6 were purchased from eBioscience (San Diego, CA). Purified anti-mouse IL-17 mAb (TC11-18H10.1), biotin-conjugated anti-mouse IL-17 mAb (TC11-8H4), and recombinant mouse IL-17 were purchased from BioLegend (San Diego, CA). For immuno-fluorescence studies, the following mAbs were used: PE-conjugated anti-mouse CD3 mAb (17A2), which recognizes T cell receptor-associated complex present on all mature T cells; PE-Cy5-conjugated anti-mouse CD4 mAb (H129.19), which recognizes protein on helper T cells; FITC-conjugated anti-mouse CD8a mAb (53-6.7), which recognizes protein on cytotoxic T cells; FITC-conjugated anti-mouse CD19 mAb (1D3), which recognizes protein on B cells; FITC-conjugated anti-mouse CD25 mAb (PC61.5), which recognizes activated T and B lymphocytes; PE-Cy5-conjugated anti-mouse CD38 mAb (90), which recognizes protein on mature B cells and plasma cells; PE-conjugated anti-mouse Foxp3 mAb (FJK-16s), which recognizes Foxp3 expressed in Treg cells (these antibodies were purchased from eBioscience, San Diego, CA).

2.7. Phenotyping of lymphocytes

Immunophenotyping of splenic lymphocytes was carried out using a FACS-LSR flow cytometer (Becton Dickinson, San Jose, CA). Spleens were harvested from normal mice and DTH mice with or without nano-C_{60} treatment. Each spleen was minced with scissors, and a single-cell suspension was prepared. Splenocytes were purified by means of hemolysis, counted under a microscope, and suspended in RPMI1640-based buffer (containing 102 mM NaCl, 5 mM KCl, 0.4 mM $CaCl_2$, 0.4 mM $MgSO_4$, 23.8 mM $NaHCO_3$, 5.6 mM Na_2HPO_4, 11.1 mM glucose and 10 mM HEPES-NaOH; pH 7.4) at a concentration of 2×10^6 cells/mL. Cells were stained with fluorochrome-conjugated antibodies for 30 min, then washed. Analysis of 10,000 lymphocyte events per tube was performed using Cell Quest software (Becton Dickinson, San Jose, CA, USA).

2.8. Determination of IFN-γ, IL-4, TNF-α, IL-6, and IL-17

Splenocytes were prepared from normal mice and DTH mice with or without nano-C_{60} treatment. The cells were suspended in RPMI1640 medium containing 10% FBS at a concentration of 7×10^6 cells/mL and cultured with mBSA (20 mg/mL) in 96-well plates. After incubation at 37 °C under an atmosphere of 5% CO_2 for 96 h, the culture supernatant was harvested for determination of IFN-γ, IL-4, TNF-α, IL-6,

and IL-17. The concentrations of IFN-γ, IL-4, TNF-α, IL-6, and IL-17 were measured by ELISA as follows. A 96-well plate was coated with purified anti-mouse IFN-γ (1:500), IL-4 (1:250), TNF-α (1:500), IL-6 (1:500), or IL-17 (1:250) mAb, and incubated overnight at 4 °C. The wells were washed with PBS containing 0.05% Tween-20, and nonspecific binding was blocked with PBS containing 1% bovine serum albumin for 1 h at room temperature. The plate was washed, and the culture supernatant was kept for 2 h at room temperature. The plate was washed again, and anti-mouse biotin-conjugated TNF-α (1:1000), IFN-γ (1:500), IL-4 (1:1000) IL-6 (1:500), or IL-17 (1:500) mAb was added for 1 h at room temperature. The plate was further washed, and avidin-horseradish peroxidase (Sigma, St. Louis, USA) was added. The plate was incubated for 30 min at room temperature, then washed, and 3,3′,5,5′-tetramethylbenzidine was added for 10–30 min. The reaction was stopped by adding 2.5 M H_2SO_4, and the absorbance at 450 nm was measured with an ImmunoReader NJ-2000 (Nihon InterMed, Tokyo, Japan). Standard curves were established with recombinant mouse IFN-γ, IL-4, TNF-α, IL-6, and IL-17, and the concentrations were estimated from the standard curves.

2.9. Effect of nano-C_{60} on cytokine productivity of splenocytes prepared from normal mice

Splenocytes were harvested from normal and DTH mice in the same way as previously described. T cells in splenocytes were activated by plate-bound anti-CD3 mAb (1 mg/mL) for 24 h and cultured with or without 30 μL of mBSA (10 mg/mL) and 100 μL of nano-C_{60} (5 mg/mL) at a concentration of 2×10^6 cells/mL in a 24-well plate at 37 °C for 96 h. After incubation, cells were harvested and cytokines in the culture supernatant were measured with ELISAs.

2.10. Analysis of regulatory T (Treg) cells

Splenocytes were prepared from normal and DTH mice with or without nano-C_{60} treatment. Cells (5×10^6 cells) were stained with PE-Cy5-conjugated anti-CD4 and FITC-conjugated anti-CD25 antibodies for Treg cell analysis for 30 min at room temperature, washed with RPMI1640-based buffer, fixed with 4% para-formaldehyde for 10 min on ice, and then treated with 0.1% Triton X-100 for 5 min at 4 °C. After having been washed with RPMI1640-based buffer and blocked with 1% BSA/PBS for 30 min at room temperature, the samples were stained with PE-conjugated anti-Foxp3 for Treg cells for 1 h at room temperature, and washed with RPMI1640-based buffer. Analysis of 10,000 lymphocyte events per tube was performed using Cell Quest software (Becton Dickinson, San Jose, CA, USA).

2.11. Statistical analysis

Values are given as mean ± S.E. Comparison between two values was performed by use of the unpaired Student's *t*-test. Multiple groups were compared using ANOVA followed by pairwise comparisons with Bonferroni's *post hoc* analysis. The criterion of a significant difference was set at $P < 0.05$. Calculations were done with the Instat version 3.0 statistical package (GraphPad Software, San Diego, CA).

3. Results

The C_{60} particles were crystalline (simple hexagonal) with an estimated mean diameter of 165 nm (Fig. 1A), and their UV spectrum was similar to that of commercial C_{60} (peaks at 270 nm, 330 nm; Fig. 1B), although there was a slight displacement of peaks.

DTH was induced in C57BL/6 mice by immunization with mBSA. The footpad swelling reached maximum at 24 h after challenge (data not shown). Normal mice and mice treated only with nano-C_{60} showed no swelling. The footpad swelling was significantly reduced in DTH mice treated with nano-C_{60}, compared with DTH-disease control mice (Fig. 2), suggesting that nano-C_{60} treatment attenuates the pathology of DTH.

Production of cytokines, including IFN-γ, IL-4, TNF-α, IL-6, and IL-17, was then examined (Fig. 3). IFN-γ production was significantly increased in DTH mice compared with the normal-control group, and nano-C_{60} treatment had no effect on this. IL-4 production was significantly increased in DTH mice, and this increase was significantly suppressed by nano-C_{60} treatment. The levels of IL-6 and IL-17 were also significantly increased in DTH mice, and nano-C_{60} treatment significantly suppressed both increases. Production of TNF-α was increased in DTH mice, and the increase was significantly further elevated by nano-C_{60} treatment (Fig. 4). The suppression of IL-17 level by nano-C_{60} was confirmed in an *in vitro* culture assay (Fig. 5). There was no significant difference in production of other cytokines between the *in vitro* assay systems with and without nano-C_{60} (data not shown).

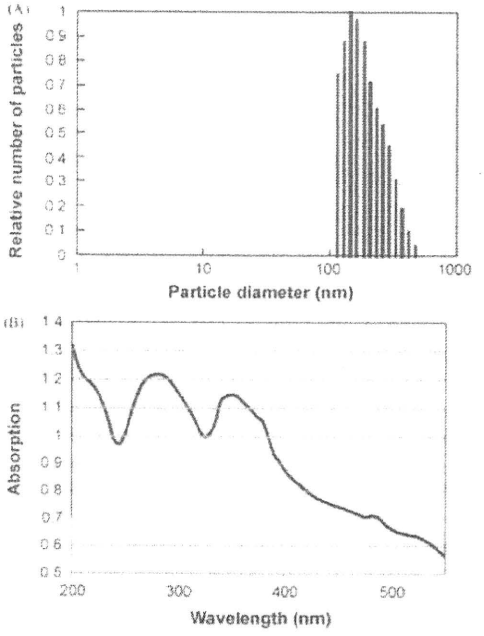

Fig. 1. Particle diameter distribution (A) and UV–vis absorbance spectrum (B) of nano-C_{60} aggregates in water.

Nano-C_{60} treatment had no significant effect on various populations of splenic lymphocytes in normal or DTH mice, as shown in Fig. 6. However, when changes in the population of Treg cells were examined, the elevated population ratio observed in the DTH-disease control group was significantly further increased by nano-C_{60} treatment (Fig. 7). These results indicate that nano-C_{60} induces up-regulation of Treg cells via the suppression of IL-17 production.

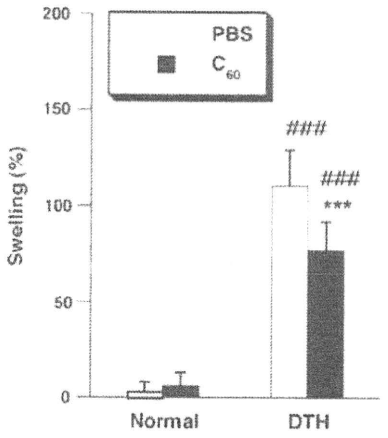

Fig. 2. Footpad swelling in DTH-disease control and nano-C_{60}-treated DTH-mice. Each value represents the mean ± S.E. ($n = 5$). DTH, delayed-type hypersensitivity; PBS, phosphate-buffered saline; C_{60}, nano-C_{60}. ### Statistically significant difference ($P < 0.005$) compared to the normal control group. *** Statistically significant difference ($P < 0.005$) compared to the DTH-disease control group.